

Numerical Simulations of Gravitational Waves from Early-Universe Turbulence

Alberto Roper Pol,^{1,2,3,*} Sayan Mandal,^{4,3} Axel Brandenburg,^{2,4,5,6,7} Tina Kahniashvili,^{4,8,3} and Arthur Kosowsky⁹

¹*Department of Aerospace Engineering Sciences, University of Colorado, Boulder, CO 80303, USA*

²*Laboratory for Atmospheric and Space Physics, University of Colorado, Boulder, CO 80303, USA*

³*Abastumani Astrophysical Observatory, Ilia State University,
3-5 Cholokashvili Ave, Tbilisi, GE-0194, Georgia*

⁴*McWilliams Center for Cosmology and Department of Physics,
Carnegie Mellon University, 5000 Forbes Ave, Pittsburgh, PA 15213, USA*

⁵*Nordita, KTH Royal Institute of Technology and Stockholm University, Roslagstullsbacken 23, 10691 Stockholm, Sweden*

⁶*Department of Astronomy, AlbaNova University Center, Stockholm University, 10691 Stockholm, Sweden*

⁷*JILA, University of Colorado, Boulder, CO 80303, USA*

⁸*Department of Physics, Laurentian University, Ramsey Lake Road, Sudbury, ON P3E 2C, Canada*

⁹*Department of Physics and Astronomy, University of Pittsburgh, and Pittsburgh Particle Physics,
Astrophysics, and Cosmology Center (PITT PACC), Pittsburgh PA 15260*

(Dated: November 15, 2019, Revision: 1.10)

We perform direct numerical simulations of magnetohydrodynamic turbulence in the early universe and numerically compute the resulting stochastic background of gravitational waves and relic magnetic fields. These simulations do not make the simplifying assumptions of earlier analytic calculations. At frequencies below the peak value, our results predict a new universal form of the gravitational wave spectrum with more power than previously suggested. The efficiency of gravitational wave production varies significantly with the physical characteristics of the turbulence. For the same amount of turbulent energy, we find that the gravitational wave signal is stronger for irrotational than for solenoidal sources. In particular, if produced at the electroweak scale, it would be detectable by the planned Laser Interferometer Space Antenna if at least 1% of the total energy density is injected into magnetic fields or turbulent plasma motions. Our results suggest that the obtained low frequency tail increases the detection prospects of gravitational waves produced over a wide range of energy scales at which turbulence might be present in the early universe.

PACS numbers: 98.70.Vc, 98.80.-k

A period of turbulence in the early universe can produce a stochastic background of gravitational waves (GWs). Turbulence might arise from the dynamics of a first-order phase transition [1–3], or from the evolution of primordial magnetic fields [4–7] coupled to the highly conducting primordial plasma. Analytic estimates suggest that turbulence generated by an electroweak phase transition can produce GWs within the detectable amplitude and frequency range of the Laser Interferometer Space Antenna (LISA) if the turbulent energy density is roughly one percent of the total energy density of the universe at that time [8–11].

The aforementioned analytic estimates make a number of simplifying assumptions. Turbulence is assumed to be hydrodynamic with a typical Kolmogorov power spectrum and a duration set by a small fraction of the Hubble time, omitting the effect of the expansion of the universe during the turbulent period. The inclusion of magnetic fields can extend the frequency range of the resulting GWs due to the transfer of power to larger scales [4, 12, 13]. These turbulence models depend on the correlation function of the turbulent velocity field with time, which is assumed in earlier works, and not

computed from magnetohydrodynamic (MHD) simulations. An accurate treatment of these effects can be essential for establishing the detectability of primordial GWs with upcoming GW detectors and, in particular, to determine the spectral shape of the resulting signals [14]. A proper understanding of turbulent sourcing of GWs is especially relevant for using LISA to constrain the parameter space of a first-order phase transition [15]. If primordial magnetic fields were present during the early universe, they could dynamically enhance turbulent plasma motions and serve as an additional source of GWs [16–18]. Such magnetic fields can persist until the present epoch. Lower bounds on their strength are suggestive of their existence [19].

Numerical simulations are required to improve on the analytic estimates. We present in this Letter the results of direct numerical simulations of magnetohydrodynamic turbulence and the resulting stochastic GW spectra. These are the first numerical results of GW production due to MHD turbulence [20]. We assume the evolution of the background universe to be described by the spatially flat, homogeneous and isotropic Friedmann-Lemaître-Robertson-Walker metric.

The expansion of the universe leads to a dilution of radiation energy density and magnetic fields, and to the damping of the GW amplitude. To scale out effects of expansion, we use comoving coordinates \boldsymbol{x} , conformal time

*Electronic address: Alberto.RoperPol@colorado.edu

t , and comoving MHD fields, such that the stress tensor T_{ij} is scaled with the scale factor a^4 . In addition, all variables are normalized with respect to their values at the starting time of the turbulence period, as described in Refs. [21–23]. This facilitates the application of our results to different scenarios of GW generation within the radiation dominated epoch in the early universe. We also use tensor-mode perturbations h_{ij} scaled with a to simplify the GW equation [24].

The full set of relativistic MHD equations is then similar to the usual MHD equations [4, 7, 23, 33], and the resulting normalized GW equation, valid only while the universe is dominated by radiation, is [21, 22]

$$(\partial_t^2 - \nabla^2)h_{ij}(\mathbf{x}, t) = 6T_{ij}^{\text{TT}}(\mathbf{x}, t)/t, \quad (1)$$

where the scaled strains, $h_{ij}(\mathbf{x}, t)$, are tensor-mode perturbations over the background metric, such that the spatial components of the total metric tensor are $g_{ij}(\mathbf{x}, t) = a^2(t)\delta_{ij} + a(t)h_{ij}(\mathbf{x}, t)$, and $T_{ij}^{\text{TT}}(\mathbf{x}, t)$ is the transverse and traceless projection of the stress tensor [34].

Starting with initial conditions for the plasma velocity and magnetic fields at the electroweak scale, we numerically solve for the dynamics of early universe MHD turbulence governed by the equations described in Ref [23], using the PENCIL CODE [35]. At each time step, we compute the spatial Fourier components of the stress tensor of a relativistic perfect fluid,

$$T_{ij} = \frac{4}{3} \frac{\rho u_i u_j}{1 - u^2} - B_i B_j + (\rho/3 + \mathbf{B}^2/2)\delta_{ij}, \quad (2)$$

where $\rho(\mathbf{x}, t)$ is the plasma energy density, $\mathbf{u}(\mathbf{x}, t)$ is the plasma velocity, and $\mathbf{B}(\mathbf{x}, t)$ is the magnetic field.

To compute the resulting GW production, we evolve the strains in Fourier space using Equation (1), assuming a constant source term during each time step of the MHD evolution. This assumption is good for time steps small enough to guarantee numerical stability of the MHD equations, and allows larger time steps than required by direct numerical simulation; see Ref. [21] for a discussion of this method, described in their section 2.6 as approach II. We run our simulations until the resulting GW spectra are stationary in comoving variables, which is well within the radiation dominated era.

To study the sensitivity to initial conditions, we have performed several sets of simulations with different physical models for driving plasma motions. The motivation for the different types of primordial magnetic fields obtained below is given in Ref. [7], where their subsequent evolution and observational constraints are discussed. The physical magnetic diffusivity η of the early universe is much smaller than what we can accurately simulate [23]. We fix the viscosity $\nu = \eta$ and choose both to be as small as possible so as not to cause numerical artifacts [7]. If the much smaller physical values were used instead, the inertial range of the turbulence would extend to higher

frequencies, but those are of little observational interest since the GW amplitude at those frequencies would be very low.

Our full set of runs is summarized in Table I. For all of the calculations, we assume $\mathbf{u}(\mathbf{x}) = \mathbf{0}$ initially. In Set I (runs ini1–3), $\mathbf{B}(\mathbf{x})$ is initialized as a fully helical (indicated by “y” under “hel”) gaussian random field with magnetic energy spectrum $\Omega_M(k) \propto k^5$ (defined as in Refs. [27, 36] and normalized as described in Refs. [21–23]) for $k < k_*$, corresponding to a solenoidal causally generated field, and $\Omega_M(k) \propto k^{-2/3}$ (Kolmogorov spectrum) for $k > k_*$, where k_* is the wave number at which the magnetic energy is injected. In Set II (runs hel1–4 and noh1–2), $\mathbf{B}(\mathbf{x}) = \mathbf{0}$ initially, but it is then numerically driven by applying an electromotive force \mathcal{E}_0 during $1 \leq t \leq t_{\text{max}}$ in the induction equation consisting of random, nearly monochromatic waves around wave number k_* [23], and we compute the decaying MHD turbulent motions, with no forcing term, for times $t > t_{\text{max}}$; see Table I for values of \mathcal{E}_0 and t_{max} . The driving force field is taken as either fully helical (runs hel1–4) or non-helical (noh1–2). The initial number of eddies per horizon length at the driving scale is $N \equiv k_*/2\pi$, usually taken to be between 1 and 100 for the first-order electroweak phase transition [37]. We arrange the simulations such that the maximum total magnetic energy density, Ω_M^{max} , integrated over all wave numbers, is a specified fraction of the radiation energy density. We take values in the range 10^{-3} to 10^{-1} . The lower limit is required for the turbulence to be the dominant source of GWs during a first-order phase transition according to analytic estimates [38], and the higher limit is imposed on magnetic fields due to their effect on Big Bang nucleosynthesis [39, 40]. Recently, values up to 10% have been obtained for magnetogenesis lattice simulations [41].

We also consider Set III (runs ac1–3) with initial

TABLE I: Summary of runs.

Run	$\mathcal{E}_0, \mathcal{F}_0$	η	Ω_i^{max}	$\Omega_{\text{GW}}^{\text{sat}}$	i	hel	t_{max}	N
ini1	—	5e-6	1.16e-01	2.05e-09	M	y	1.00	100
ini2	—	5e-8	7.62e-03	6.38e-12	M	y	1.00	100
ini3	—	5e-7	7.62e-03	6.36e-10	M	y	1.00	10
hel1	1.4e-3	5e-7	2.17e-02	4.43e-09	M	y	1.10	100
hel2	8.0e-4	5e-7	7.18e-03	4.67e-10	M	y	1.10	100
hel3	2.0e-3	5e-7	4.62e-03	2.09e-10	M	y	1.01	100
hel4	1.0e-4	2e-6	5.49e-03	1.10e-11	M	y	1.01	1000
noh1	1.4e-3	5e-7	1.44e-02	3.10e-09	M	n	1.10	100
noh2	8.0e-4	2e-6	4.86e-03	3.46e-10	M	n	1.10	100
ac1	3.0	2e-5	1.33e-02	5.66e-08	K	n	1.10	100
ac2	3.0	5e-5	1.00e-02	3.52e-08	K	n	1.10	100
ac3	1.0	5e-6	2.87e-03	2.75e-09	K	n	1.10	100

$\mathbf{B}(\mathbf{x}) = \mathbf{u}(\mathbf{x}) = \mathbf{0}$, using irrotational or “acoustic” hydrodynamic turbulence sourced by a gradient of random Gaussian potentials [31]. In this case, the forcing \mathcal{F}_0 appears as an additional term in the momentum equation, which acts during $1 \leq t \leq t_{\max}$ [23].

We choose solenoidal and irrotational forcing fields in Sets II and III, respectively, for comparison purposes. In all of our runs, the size of the cubic domain L is taken to be $L = 2\pi/N$, such that the lower wave number in the computed spectra corresponds to N . We evolve the dynamical equations on a mesh of 1152^3 mesh of grid points.

Figure 1 shows the resulting magnetic field and GW energy spectra for a case of strong turbulence. The $k^{-5/3}$ inertial range in the magnetic field corresponds to $k^{-11/3}$ in the GW energy density, defined as in Refs. [22, 27]. This is expected because the stress from a magnetic field with a spectrum following a certain power law in its inertial range has again the same power law [42]. This results in a GW spectrum that asymptotically falls off faster by a k^2 factor than the spectrum of the source, i.e., $\Omega_{\text{GW}}(k) \propto \Omega_{\text{M}}(k)/k^2$, as inferred from Equation (1). The GW spectrum for wave numbers below the spectral peak, $k_{\text{GW}} \approx 2k_*$, becomes essentially constant. This small- k behavior in $\Omega_{\text{GW}}(k)$ can be traced back to a white noise spectrum of the magnetic stress, which seems to emerge even when the magnetic field itself has a spectrum $\Omega_{\text{M}}(k)/k$ steeper than k^2 in the subinertial range [42]. For such spectrum, the corresponding GW spectrum $\Omega_{\text{GW}}(k)/k$ should scale with k^0 , i.e., constant, as we observe in our simulations (see Figure 1). This argument proves that the expected scaling of $\Omega_{\text{GW}}(k)/k$ with k^2 obtained in previous analytical estimates as in, e.g., Ref. [11], cannot hold [43]. We suggest that the reason could be that in previous works the power increase of the magnetic field energy density at low- k tails due to non-helical transfer [45, 46] was neglected. It is only during the first few oscillations that the GW spectrum is still proportional to k^2 , until the k^0 scaling extends over the range between the stirring scale and the lower wave number in our simulations. We always observe the development of this flat spectrum using different numerical domains. This rules out the possibility of this scaling to be due to numerical artifacts. The time it takes for the change of slope to occur below the horizon scale is much smaller than the time it takes for the GW spectrum to become stationary. Therefore, we conclude that the $+2$ slope is not relevant for the characterization of the signal [44].

The GW energy density $h_0^2 \Omega_{\text{GW}}(f)$ evaluated at the present time, as a function of frequency f , and the characteristic strain amplitude $h_c(f)$, defined as in Refs. [22, 27], are shown in Figure 2 for runs ini1–3. These are obtained by scaling the computed variables to our present time, as described in Ref. [22]. For GWs generated at the electroweak scale, we take the values $T_* = 100 \text{ GeV}$

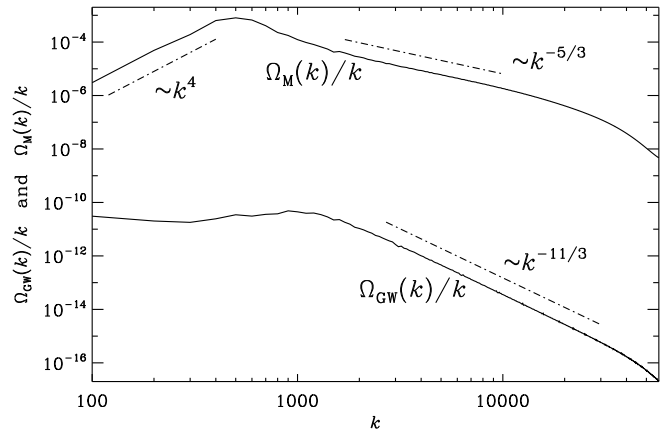


FIG. 1: Magnetic and GW energy spectra for run ini2 averaged over late times ($t > 1.1$), after the GW spectrum oscillates around a stationary state, with $\Omega_{\text{M}}^{\text{max}} \approx 0.12$ and $\Omega_{\text{GW}}^{\text{sat}} \approx 2 \times 10^{-9}$. Note that spectra and wave numbers are normalized with the radiation energy density and the Hubble scale at the time of generation [22].

for the temperature, and $g_* \approx g_{\text{S}} = 100$ for the number of relativistic and adiabatic degrees of freedom. For different values, the results scale in the following way: the frequency would shift proportional to $T g_*^{1/2} g_{\text{S}}^{-1/3}$, the strain amplitude varies with $T^{-1} g_{\text{S}}^{-1/3}$, and the GW energy density with $g_* g_{\text{S}}^{-4/3}$. Likewise, the GW strain amplitude is proportional to the stirring scale $N^{-3/2}$ and the frequency is proportional to N [11]. The slopes of $\Omega_{\text{GW}}(f)$ are consistent with those of $\Omega_{\text{GW}}(k)/k$ in Figure 1, since $2\pi f = ck$ for GWs. The spectrum of $h_c(f)$ shows scaling with $f^{-1/2}$ for low frequencies and with $f^{-7/3}$ in the inertial range. This corresponds to the estimated scaling $h_c(f) \propto \sqrt{\Omega_{\text{GW}}(f)/f^2}$. As previously, we expect the subinertial slope of $-1/2$ to eventually turn over a slope of $+1/2$. However, this slope is not observed in sub-Hubble scales.

In runs ini1–3, GWs are produced by the sudden emergence of a magnetic field. In reality, this will be a gradual process, as modeled by Sets II and III of runs. The time evolution of Ω_i (for $i = \text{GW}, \text{K}, \text{or M}$), integrated over all wave numbers, is shown in Figure 3 for ini1–3, hel1–2, and ac1. In all cases, the GW energy density saturates at a value $\Omega_{\text{GW}}^{\text{sat}}$ shortly after the sourcing energy density has reached its maximum value $\Omega_{\text{M,K}}^{\text{max}}$; see Table I.

We observe in Figure 4 that runs hel1–3, noh1, and ac1 present steeper GW spectra at high frequencies than in runs ini1–3. The monochromatic forcing produces a spike in $\Omega_{\text{M}}(f)$ at f_* and a sharp drop in $\Omega_{\text{GW}}(f)$ and $h_c(f)$ beyond $f_{\text{GW}} \approx 2f_*$, for the magnetic runs. For the acoustic runs, we observe a smooth bump on the spectra of $\Omega_{\text{GW}}(f)$ and $h_c(f)$, near the spectral peak f_* . Again, the spectra have the same low frequency tail, which underlines its universal nature. Interestingly, for given in-

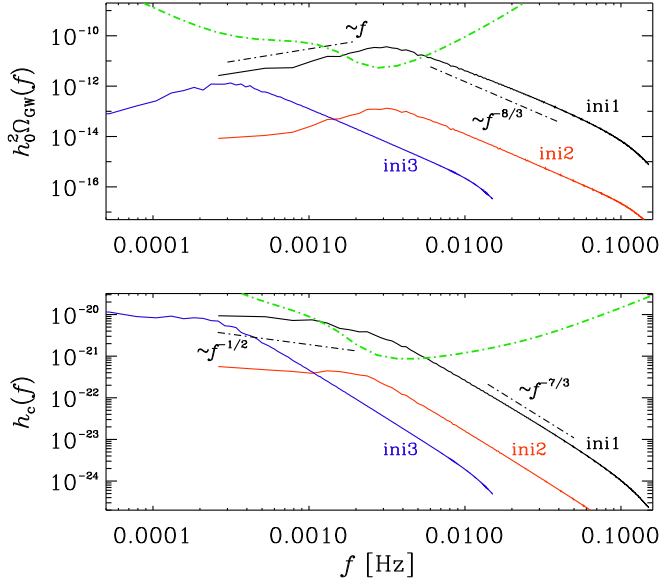


FIG. 2: Spectra of $h_0^2 \Omega_{\text{GW}}(f)$ and $h_c(f)$, evaluated at the present time, along with the LISA sensitivity curve (green dot-dashed line) to a stochastic GW background after 4 years of mission [47, 48]. Note that ini1–3 differ in the initial total energy density of the magnetic fields and the peak wave number (see table I for values).

put energy, $\Omega_{\text{M,K}}^{\text{max}}$, the largest value of $\Omega_{\text{GW}}^{\text{sat}}$ is obtained for acoustic turbulence. This case was already studied in Refs. [13, 15, 49].

For a given type of initial condition and stirring scale, the final energy density in GWs has the expected quadratic dependence on the source energy density to a very good approximation as shown in Figure 5. The efficiency of GW production varies significantly with the type of initial conditions; for the same total source energy, the cases with forced acoustic compression lead to a factor of around 2000 more GW energy than the sudden magnetic field (ini1–3), while the cases with forced non-helical magnetic fields are 100 times more efficient. We also observe that non-helical forcing fields are about a factor of 1.6 more efficient than helical magnetic fields. The detailed reasons behind these significant variations in efficiency are unclear, but they imply that accurate predictions of GW production from cosmological phase transitions will require a detailed model of how latent heat is converted to plasma and magnetic field energies. The comparison of efficiency in GW generation between acoustic and rotational turbulence is a subject of further investigation.

The projected sensitivity curve for the LISA space mission [47, 48] was plotted in Figures 2 and 4 along with GW spectra from our runs. The cases ini2–3, each with a turbulent energy input of around 1% of the total radiation energy density produce GW amplitudes below LISA’s sensitivity, while ini1, with a turbulent energy in-

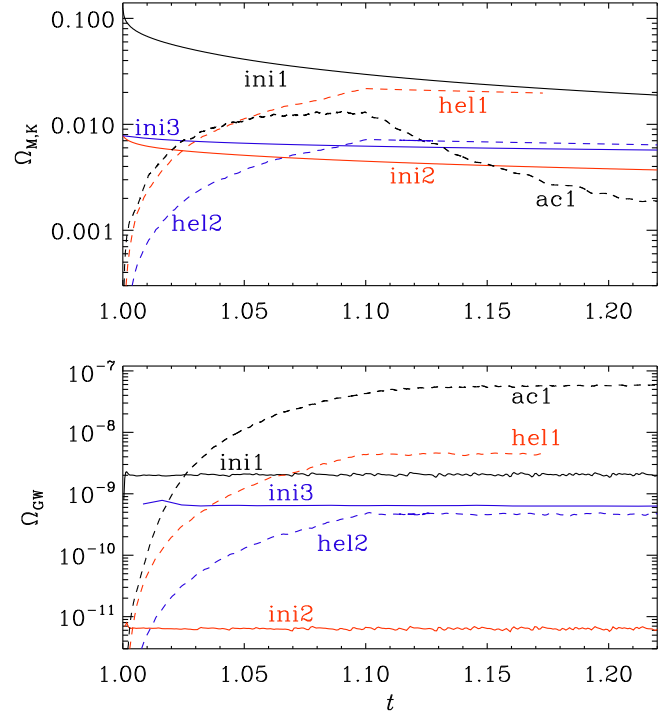


FIG. 3: Evolution of $\Omega_{\text{M,K}}$ (top) and Ω_{GW} (bottom) for runs with initial energy (ini1–3) and runs where energy is driven through monochromatic forcing (hel1–2 and ac1). Note that the energy densities are normalized with the radiation energy density at the time of generation [22].

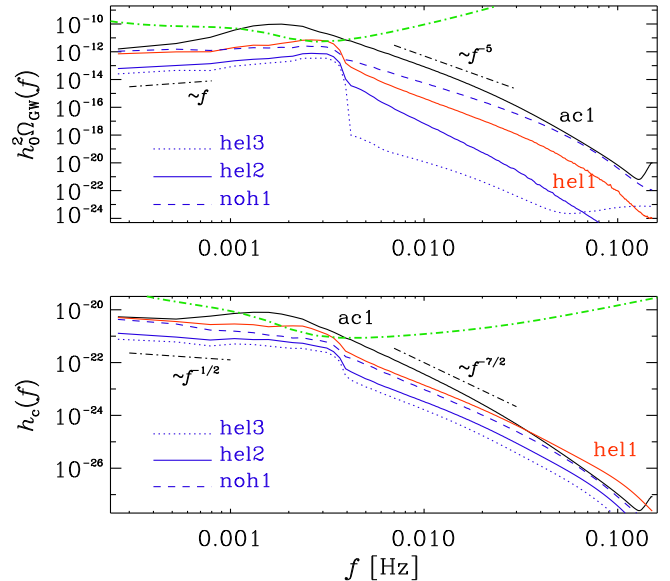


FIG. 4: Similar to Figure 2, but for runs hel1–3, noh1, and ac1.

put of around 10% could be detectable. An energy input of about 3% is required to obtain a GW spectrum above

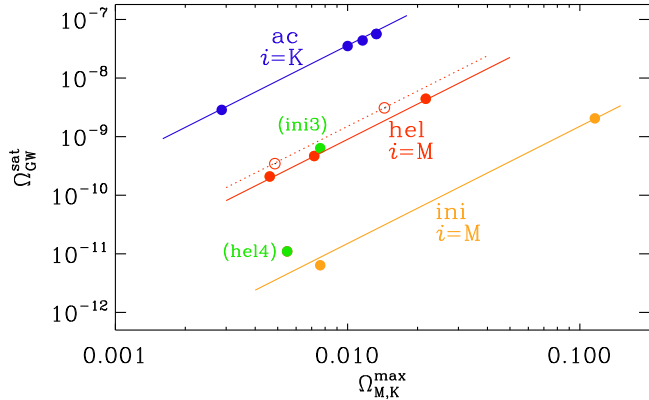


FIG. 5: $\Omega_{\text{GW}}^{\text{sat}}$ versus $\Omega_{\text{M,K}}^{\text{max}}$. The quadratic dependency, inferred from the +2 slope of the lines, holds within runs of the same type. Note that runs ini3 ($N = 10$) and hel4 ($N = 1000$), in green, have different stirring scales than the rest of the runs ($N = 100$).

LISA's peak sensitivity for runs with an initial helical magnetic field. On the other hand, the runs with forced magnetic fields would peak above LISA for an energy input of approximately 2% for non-helical forcing, and 3% for helical forcing, according to our results. Acoustic forced turbulence has been shown to be the more efficient case considered, even though it leads to a GW spectral peak closer to the forcing peak, which slightly reduces the prospects of detection for $T_* = 100 \text{ GeV}$ and $N = 100$. An energy input of around 0.3% would be enough in this case for GW spectrum to peak over LISA's sensitivity.

The novel $f^{-1/2}$ low frequency spectrum for $h_c(f)$ demonstrated here enhances the detectability compared to the $f^{1/2}$ spectrum obtained from earlier analytic models typically assumed in recent analyses as, e.g., in Ref. [50]. Now scheduled for launch in the mid 2030's, LISA may provide crucial insight into fundamental physics during the first picoseconds of cosmic evolution.

Support through the NSF Astrophysics and Astronomy Grant Program (grants 1615940 & 1615100), and the Shota Rustaveli NSF (Georgia) (grant FR/18-1462) are gratefully acknowledged. We acknowledge the allocation of computing resources provided by the Swedish National Allocations Committee at the Center for Parallel Computers at the Royal Institute of Technology in Stockholm.

[1] M. Kamionkowski, A. Kosowsky, and M. S. Turner, Phys. Rev. D **49**, 2837 (1994).

[2] E. Witten, Phys. Rev. D **30**, 272 (1984).

[3] C. J. Hogan, Mon. Not. Roy. Astron. Soc. **218**, 629

(1986).

- [4] A. Brandenburg, K. Enqvist, and P. Olesen, Phys. Rev. D **54**, 1291 (1996).
- [5] M. Christensson, M. Hindmarsh, and A. Brandenburg, Phys. Rev. E **64**, 056405 (2001).
- [6] T. Kahniashvili, A. Brandenburg, A. G. Tevzadze, and B. Ratra, Phys. Rev. D **81**, 123002 (2010).
- [7] A. Brandenburg, T. Kahniashvili, S. Mandal, A. Roper Pol, A. G. Tevzadze, and T. Vachaspati, Phys. Rev. D **96**, 123528 (2017).
- [8] A. Kosowsky, A. Mack, and T. Kahniashvili, Phys. Rev. D **66**, 024030 (2002).
- [9] T. Kahniashvili, G. Gogoberidze, and B. Ratra, Phys. Rev. Lett. **95**, 151301 (2005).
- [10] C. Caprini and R. Durrer, Phys. Rev. D **74**, 063521 (2006).
- [11] G. Gogoberidze, T. Kahniashvili, and A. Kosowsky, Phys. Rev. D **76**, 083002 (2007).
- [12] A. Pouquet, U. Frisch, and J. Léorat, J. Fluid Mech. **77**, 321 (1976).
- [13] P. Niksa, M. Schlexer, and G. Sigl, Class. Quant. Grav. **35**, 144001 (2018).
- [14] J. D. Romano and N. J. Cornish, Living Rev. Rel. **20**, 2 (2017).
- [15] M. Hindmarsh, S. J. Huber, K. Rummukainen, and D. J. Weir, Phys. Rev. D **96**, 103520 (2017).
- [16] D. V. Deryagin, D. Y. Grigoriev, V. A. Rubakov, and M. V. Sazhin, Mon. Not. R. Astron. Soc. **229**, 357 (1987).
- [17] T. Kahniashvili, G. Gogoberidze, and B. Ratra, Phys. Rev. Lett. **100**, 231301 (2008).
- [18] C. Caprini, R. Durrer, and G. Servant, JCAP **0912**, 024 (2009).
- [19] A. Neronov and I. Vovk, Science **328**, 73 (2010).
- [20] C. Caprini *et al.*, arXiv:1910.13125 (2019).
- [21] A. Roper Pol, A. Brandenburg, T. Kahniashvili, A. Kosowsky, and S. Mandal, Geophys. Astrophys. Fluid Dynam., DOI:10.1080/03091929.2019.1653460 (2019).
- [22] See Supplemental Material, Sec. 1, which includes Refs. [21, 23–28], for the details on the normalization of the gravitational wave equation.
- [23] See Supplemental Material, Sec. 2, which includes Refs. [4, 7, 21, 22, 27, 29–32], for the set of MHD equations used for the early universe.
- [24] L. P. Grishchuk, Sov. Phys. JETP **40**, 409 (1974).
- [25] V. F. Mukhanov, H. A. Feldman, and R. H. Brandenberger, Phys. Rep. **215**, 203 (1992).
- [26] A. Friedmann, *Zeitschrift für Physik*, **10**, 377 (1922).
- [27] M. Maggiore, Phys. Rep. **331**, 283 (2000).
- [28] K. Saikawa and S. Shirai, JCAP **05**, 035 (2018)
- [29] A. Brandenburg, Astrophys. J. **550**, 824 (2001).
- [30] A. Brandenburg, W. Dobler, and K. Subramanian, Astron. Nachr. **323**, 99 (2002).
- [31] A. J. Mee and A. Brandenburg, Mon. Not. R. Astron. Soc. **370**, 415 (2006).
- [32] A. Brandenburg *et al.*, Astrophys. J. **845**, L21 (2017).
- [33] R. Durrer and A. Neronov, Astron. Astrophys. Rev. **21**, 62 (2013).
- [34] C. Misner, K. Thorne, and J. A. Wheeler, W. H. Freeman (1973).
- [35] The PENCIL CODE, <https://github.com/pencil-code>, DOI:10.5281/zenodo.2315093
- [36] R. Durrer and C. Caprini, J. Cosmol. Astropart. Phys. **0311**, 010 (2003).
- [37] M. S. Turner, E. J. Weinberg, and L. M. Widrow, Phys.

- Rev. D **46**, 2384 (1992).
- [38] A. Nicolis, *Class. Quant. Grav.* **21**, L27 (2004).
- [39] T. Kahniashvili, A. G. Tevzadze, and B. Ratra, *Astrophys. J.* **726**, 78 (2011).
- [40] D. G. Yamazaki and M. Kusakabe, *Phys. Rev. D* **86**, 123006 (2012).
- [41] Y. Zhang, T. Vachaspati, and F. Ferrer, *Phys. Rev. D* **100**, 083006 (2019).
- [42] See Supplemental Material, Sec. 3, which includes Ref. [23], for a demonstration that a field with a blue k^4 spectrum always yields a white noise k^2 spectrum of the source.
- [43] See Supplemental Material, Sec. 4, which includes Refs. [11, 42, 44], for a comparison with the spectrum obtained in Ref. [11].
- [44] See Supplemental Material, Sec. 5, which includes Refs. [22, 42, 43], for a demonstration of the k^2 sub-inertial range in $\Omega_{\text{GW}}(k, t)/k$ at early times.
- [45] A. Brandenburg, T. Kahniashvili, and A. G. Tevzadze, *Phys. Rev. Lett.* **114**, 075001 (2015).
- [46] A. Brandenburg and T. Kahniashvili, *Phys. Rev. Lett.* **118**, 055102 (2017).
- [47] T. Robson, N. J. Cornish, and C. Liu, *Class. Quant. Grav.* **36**, 105011 (2019).
- [48] T. L. Smith and R. Caldwell, arXiv:1908.00546 (2019).
- [49] M. Hindmarsh, S. J. Huber, K. Rummukainen, and D. J. Weir, *Phys. Rev. D* **92**, 123009 (2015).
- [50] D. Croon, V. Sanz, and G. White, *JHEP* **1808**, 203 (2018).

Supplemental Material

to “Numerical Simulations of Gravitational Waves from Early Universe Turbulence”

by Roper Pol et al.

1 Normalization of the GW equation

The normalized gravitational wave (GW) equation presented in Equation (1) of the Letter is not the standard equation that the reader might be familiar with. For this reason, we present here the details of its derivation and the corresponding consequences on the GW diagnostics; see also Ref. [21].

The spatial components of the background metric for a flat, isotropic and homogeneous universe are described by the Friedmann–Lemaître–Robertson–Walker metric: $a^2(t) \delta_{ij}$, where a is the scale factor.

Assuming small tensor-mode perturbations, $a^2(t) h_{ij}^{\text{phys}}(\mathbf{x}, t)$, over the background metric, such that the resulting metric tensor is $g_{ij}(\mathbf{x}, t) = a^2(t)[\delta_{ij} + h_{ij}^{\text{phys}}(\mathbf{x}, t)]$, the GW equation in physical space, \mathbf{x}_{phys} , and time coordinates, t_{phys} , is [24, 25]

$$\begin{aligned} & \left(\partial_{t_{\text{phys}}}^2 + 3H(t)\partial_{t_{\text{phys}}} - c^2 \nabla_{\text{phys}}^2 \right) h_{ij}^{\text{phys}}(\mathbf{x}, t) \\ & = \frac{16\pi G}{c^2} T_{ij, \text{phys}}^{\text{TT}}(\mathbf{x}, t), \end{aligned} \quad (3)$$

where c is the speed of light, G is Newton’s gravitational constant, $H(t) = (\partial_{t_{\text{phys}}} a)/a$ is the Hubble rate, $\nabla_{\text{phys}} = \partial_{\mathbf{x}_{\text{phys}}}$, and $T_{ij, \text{phys}}^{\text{TT}}(\mathbf{x}, t)$ are the transverse and traceless components of the physical stress tensor, computed from magnetohydrodynamic (MHD) equations; see Section (2).

The GW Equation (3) can be expressed in terms of comoving space coordinates $\mathbf{x} = \mathbf{x}_{\text{phys}}/a$, conformal time t , such that $dt = dt_{\text{phys}}/a$, comoving stress tensor $T_{ij}^{\text{TT}}(\mathbf{x}, t) = a^4 T_{ij, \text{phys}}^{\text{TT}}(\mathbf{x}, t)$, and scaled strains $h_{ij}(\mathbf{x}, t) = a(t) h_{ij}^{\text{phys}}(\mathbf{x}, t)$ as

$$\begin{aligned} & \left(\partial_t^2 - \frac{\partial_t^2 a}{a}(t) - c^2 \nabla^2 \right) h_{ij}(\mathbf{x}, t) \\ & = \frac{16\pi G}{a(t)c^2} T_{ij}^{\text{TT}}(\mathbf{x}, t). \end{aligned} \quad (4)$$

When the universe was dominated by radiation (approximately until the epoch of recombination), the pressure was given by the relativistic equation of state $p(\mathbf{x}, t) = \rho(\mathbf{x}, t)c^2/3$. This relation allows us to obtain the solution to the Friedmann equations [26], which results in a linear evolution of the scale factor with conformal time such that $\partial_t^2 a(t) = 0$. This simplifies Equa-

tion (4) to

$$(\partial_t^2 - c^2 \nabla^2) h_{ij}(\mathbf{x}, t) = \frac{16\pi G}{a(t)c^2} T_{ij}^{\text{TT}}(\mathbf{x}, t). \quad (5)$$

The stress tensor can be normalized as $\bar{T}_{ij}^{\text{TT}}(\mathbf{x}, t) = T_{ij}^{\text{TT}}(\mathbf{x}, t)/\mathcal{E}_{\text{rad}}^*$, where the radiation energy density during the radiation dominated epoch is equal to the total energy density of the universe, given by the critical energy density derived from the Friedmann equations,

$$\mathcal{E}_{\text{rad}}^* = \frac{\pi^2 g_*(T_*) (k_B T_*)^4}{30 (\hbar c)^3} = \frac{3H_*^2 c^2}{8\pi G}, \quad (6)$$

where T_* , $g_*(T_*)$, and H_* are the temperature, the number of relativistic degrees of freedom, and the Hubble rate, respectively, during the time of generation, and k_B and \hbar are the Boltzmann and the reduced Planck constants. If we take $T_* = 100 \text{ GeV}$ and $g_* = 100$ for the electroweak phase transition, the Hubble rate is

$$H_* \approx 2.066 \times 10^{10} \text{ s}^{-1} \left(\frac{k_B T_*}{100 \text{ GeV}} \right)^2 \left(\frac{g_*(T_*)}{100} \right)^{1/2}, \quad (7)$$

where the proportionality factors T and g_* are kept as a parameter due to the uncertainty of their exact values.

We also normalize t with respect to the conformal time of generation t_* , which corresponds to the time where the turbulent motions sourcing GWs are assumed to begin to be generated, such that $\bar{t} = t/t_*$. Due to the linear evolution of the scale factor, t_* can be related to H_* as $t_* = H_*^{-1}$, where $a_* = 1$ has been used. Note that this is different than the usual convention to set $a_0 = 1$ at the present time. This normalization allows us to express the evolution of the scale factor as $a = \bar{t}$. The space coordinates are normalized as $\bar{\mathbf{x}} = \mathbf{x}H_*/c$, and the Laplacian operator as $\bar{\nabla}^2 = \partial_{\bar{\mathbf{x}}}^2$. The GW Equation (5) reduces to the normalized GW equation.

$$(\partial_{\bar{t}}^2 - \bar{\nabla}^2) h_{ij}(\bar{\mathbf{x}}, \bar{t}) = \frac{6}{\bar{t}} \bar{T}_{ij}^{\text{TT}}(\bar{\mathbf{x}}, \bar{t}). \quad (8)$$

After removing the bars, we recover Equation (1) of the Letter. We will refer to normalized variables from now on, unless stated otherwise.

The characteristic amplitude of GWs is defined as [27]

$$h_c^2(t) = \frac{1}{2} \langle h_{ij, \text{phys}}^2(\mathbf{x}, t) \rangle, \quad (9)$$

where the angle brackets denote averaging over physical volume. In terms of scaled strains $h_{ij}(\mathbf{x}, t)$, during the radiation dominated epoch, our normalization leads to

$$h_c^2(t) = \frac{1}{2t^2} \langle h_{ij}^2(\mathbf{x}, t) \rangle. \quad (10)$$

The spectrum of the characteristic amplitude of GWs is defined following Ref. [27], such that $\int_{-\infty}^{\infty} h_c^2(k, t) d \ln k =$

$h_c^2(t)$; see details in Ref. [21]. Note that here k refers to normalized wave number \bar{k} , consistently given by $\bar{k} = ck/H_* = ack_{\text{phys}}/H_*$, where again we omit the overbar from now on. In the absence of turbulent sources, and neglecting details of the GW transfer function due to evolving relativistic degrees of freedom and transitions between radiation, matter, and dark energy dominations; see Ref. [28], the characteristic amplitude $h_c(k, t)$ dilutes due to the expansion of the universe as a^{-1} . Hence, the relic observable amplitude at the present time, $h_c(k)$, is the amplitude at the end of the simulation t_{end} , i.e., after the GW spectra oscillate around a steady state, diluted by a factor t_{end}/a_0 .

The value of the scale factor a_0 is obtained assuming adiabatic expansion of the universe, i.e., such that $g_S T^3 a^3$ is kept constant, where g_S is the number of adiabatic degrees of freedom. Our convention to set $a_* = 1$ leads to the following value for $T_* = 100 \text{ GeV}$ and $g_S \approx g_*$

$$a_0 \approx 1.254 \times 10^{15} \left(\frac{k_B T_*}{100 \text{ GeV}} \right) \left(\frac{g_S(T_*)}{100} \right)^{1/3}, \quad (11)$$

where, again, T and g_S are uncertain and kept in the expression as parameters.

The physical energy density carried by the GWs, $\mathcal{E}_{\text{GW}}(t)$, is defined as [27]

$$\mathcal{E}_{\text{GW}}(t) = \frac{c^2}{32\pi G} \langle (\partial_{t_{\text{phys}}} h_{ij}^{\text{phys}}(\mathbf{x}, t))^2 \rangle, \quad (12)$$

which can be normalized as the stress tensor, leading to $\Omega_{\text{GW}}(t) = \mathcal{E}_{\text{GW}}(t)/\mathcal{E}_{\text{rad}}^*$. In terms of conformal time t , and scaled strains $h_{ij}(\mathbf{x}, t)$, during the radiation dominated epoch, our normalization leads to

$$\Omega_{\text{GW}}(t) = \frac{1}{12t^4} \langle (\partial_t h_{ij}(\mathbf{x}, t) - h_{ij}(\mathbf{x}, t)/t)^2 \rangle. \quad (13)$$

The GW energy density spectrum $\Omega_{\text{GW}}(k, t)$ is defined as in Ref. [27], such that $\int_{-\infty}^{\infty} \Omega_{\text{GW}}(k, t) d \ln k = \Omega_{\text{GW}}(t)$; see details in Ref. [21]. This is the standard normalization that we use within the PENCIL CODE. However, when we are interested in the relic signal at the present time, e.g., when we compare our results with LISA's sensitivity in Figures 2 and 4, it is useful to normalize by the critical energy density at the present time,

$$\mathcal{E}_{\text{crit}}^0 = \frac{3H_0^2 c^2}{8\pi G}, \quad (14)$$

where $H_0 = 100 h_0 \text{ km s}^{-1} \text{ Mpc}^{-1} \approx 3.241 \times 10^{-18} h_0 \text{ s}^{-1}$ is the Hubble rate at the present time. We use $h_0^2 \Omega_{\text{GW}}$ to get rid of the uncertainties of its actual value [27], which can be obtained by multiplying the factor $(H_*/H_0)^2$ to Equation (13). The GW energy density also dilutes due to the expansion of the universe as a^{-4} . Hence, the relic observable at the present time, $\Omega_{\text{GW}}(k)$, is the energy density at the end of the simulation t_{end} , reduced by a

factor $(t_{\text{end}}/a_0)^4$. Finally, we express the GWs amplitude and energy density spectra as observables at the present time, as a function of the physical frequency, shifted to the present time, $h_c(f)$ and $\Omega_{\text{GW}}(f)$. The frequency is directly obtained as

$$f = \frac{ck_{\text{phys}}}{2\pi} = \frac{H_* a_0^{-1}}{2\pi}. \quad (15)$$

The details on the computation of its corresponding spectral function are given in Ref. [21].

2 MHD equations for the early universe

The MHD equations for an ultrarelativistic gas in a flat expanding universe [4, 7] in the radiation dominated era after the electroweak phase transition are given by

$$\begin{aligned} \frac{\partial \ln \rho}{\partial t} &= -\frac{4}{3} (\nabla \cdot \mathbf{u} + \mathbf{u} \cdot \nabla \ln \rho) \\ &\quad + \frac{1}{\rho} [\mathbf{u} \cdot (\mathbf{J} \times \mathbf{B}) + \eta \mathbf{J}^2], \end{aligned} \quad (16)$$

$$\begin{aligned} \frac{\partial \mathbf{u}}{\partial t} &= -\mathbf{u} \cdot \nabla \mathbf{u} + \frac{\mathbf{u}}{3} (\nabla \cdot \mathbf{u} + \mathbf{u} \cdot \nabla \ln \rho) \\ &\quad - \frac{\mathbf{u}}{\rho} [\mathbf{u} \cdot (\mathbf{J} \times \mathbf{B}) + \eta \mathbf{J}^2] - \frac{1}{4} \nabla \ln \rho \\ &\quad + \frac{3}{4\rho} \mathbf{J} \times \mathbf{B} + \frac{2}{\rho} \nabla \cdot (\rho \nu \mathbf{S}) + \mathcal{F}, \end{aligned} \quad (17)$$

$$\frac{\partial \mathbf{B}}{\partial t} = \nabla \times (\mathbf{u} \times \mathbf{B} - \eta \mathbf{J} + \mathcal{E}), \quad (18)$$

where $S_{ij} = \frac{1}{2}(u_{i,j} + u_{j,i}) - \frac{1}{3}\delta_{ij}\nabla \cdot \mathbf{u}$ are the components of the rate-of-strain tensor with commas denoting partial derivatives and \mathbf{J} is the current density.

Energy can be injected through ponderomotive and electromagnetic forces, \mathcal{F} and \mathcal{E} , respectively. In Set II of the runs presented in the Letter, we force helical and non-helical magnetic fields through \mathcal{E} , using the forcing term described in Refs. [29, 30]. For acoustic runs (Set III of the Letter), we use a forcing term \mathcal{F} computed as the gradient of random potentials consisting of Gaussians $\propto \exp[-(\mathbf{x} - \mathbf{x}_i)^2/R^2]$. This results in a number of eddies $N = (\pi R)^{-1}$ [31].

We use comoving variables and conformal time, all normalized to their values at the time of generation, such that the resulting stress tensor corresponds to the comoving and normalized tensor defined in Equation (2) of the Letter; see Section (1). The resulting normalized MHD variables are $\bar{\rho} = \rho c^2/\mathcal{E}_{\text{rad}}^*$, $\bar{\mathbf{u}} = \mathbf{u}/c$, $\bar{\mathbf{J}} = (c/H_*)\mathbf{J}/\sqrt{\mathcal{E}_{\text{rad}}^*}$, $\bar{\mathbf{B}} = \mathbf{B}/\sqrt{\mathcal{E}_{\text{rad}}^*}$, $\bar{\eta} = H_*\eta/c^2$, $\bar{\nu} = H_*\nu/c^2$, $\bar{\mathcal{F}} = \mathcal{F}/(H_*c)$, and $\bar{\mathcal{E}} = \mathcal{E}/\sqrt{c^2\mathcal{E}_{\text{rad}}^*}$; where the overbars have been dropped on Equations (16)–(18). In addition, ρ is scaled with the scale factor a^4 , the magnetic field amplitudes B are scaled with a^2 , and the current density J is scaled with a^3 . We have used a relativistic

equation of state $p = c_s^2\rho$, being $c_s^2 = 1/3$ the speed of sound.

The physical value of the magnetic diffusivity η at the electroweak phase transition is given in Equation (9) of Ref. [32]: $\eta \approx 4 \times 10^{-9} (k_B T_*/100 \text{ GeV})^{-1} \text{ cm}^2/\text{s}$. This corresponds to 9.2×10^{-20} in our normalized units. We set the viscosity $\nu = \eta$ in our simulations.

The energy density of magnetic and kinetic fields are computed as $\Omega_{\text{M}}(t) = \langle B^2 \rangle/2$, $\Omega_{\text{K}}(t) = \langle \rho u^2 \rangle/2$, where the angle brackets refer to physical space volume average. We define the magnetic and kinetic energy spectrum, such that $\int_{-\infty}^{\infty} \Omega_{\text{M,K}}(k, t) d \ln k = \Omega_{\text{M,K}}(t)$, in terms of logarithmic wave number intervals, for similarity with usual definition of the spectrum of GW energy density; see Ref. [27] and Section (1), and Ref. [21] for details on the computation of $\Omega_{\text{M,K}}(k, t)$.

3 Spectra of B and B^2

We show in Figure 6 the usual shell-integrated spectra of the magnetic field, $E_{\text{M}}(k)$, defined such that $\int_0^{\infty} E_{\text{M}}(k) dk = \Omega_{\text{M}}$, which is related to the spectrum defined in Section (2) as $E_{\text{M}}(k) = \Omega_{\text{M}}(k)/k$. We also show the spectrum of the stress tensor T_{ij} , $E_{\text{T}}(k)$, which is computed such that $\int_0^{\infty} E_{\text{T}}(k) dk = \langle T_{ij} T_{ij} \rangle/2$, where angle brackets denote averaging over physical volume and T_{ij} is defined in Equation (2) of the Letter. Note that this corresponds to the squared of the magnetic field, $\langle (B^2)^2 \rangle/2$, in the absence of fluid motions.

We observe that when $E_{\text{M}}(k)$ has a white noise k^2 spectrum (see Figure 6) or even a Batchelor k^4 spectrum, the stress spectrum $E_{\text{T}}(k)$ is always that of white noise. The k^4 spectrum is caused by a white noise vector potential, but the spectrum of the resulting stress can never be steeper than k^2 . We also observe the peak of the stress spectrum to shift to $2k_*$, being k_* the position of the spectral peak of the magnetic field.

The stress spectrum determines the asymptotic behavior of the spectrum of GW energy density as $\Omega_{\text{GW}}(k)/k \propto E_{\text{T}}(k)/k^2$, as inferred from Equation (1) of the Letter. Hence, the k^2 white noise spectrum results in the k^0 obtained GW spectrum $\Omega_{\text{GW}}(k)/k$, and the GW spectral peak is located at $k_{\text{GW}} \approx 2k_*$, as shown in the Letter.

In the inertial range we observe both spectra $E_{\text{M}}(k)$ and $E_{\text{T}}(k)$ to present the same Kolmogorov scaling $k^{-5/3}$.

4 Comparison with analytic approach

Looking at Figure 1 of Ref. [11], we see a peak at 1 mHz and $h_c \approx 4 \times 10^{-20}$ for their largest Mach number of unity. By comparison, for our run in1, the spectrum shows an intermediate peak at 3 mHz and $h_c \approx 0.7 \times 10^{-20}$. Our Mach number based on the Alfvén speed is just some 20%

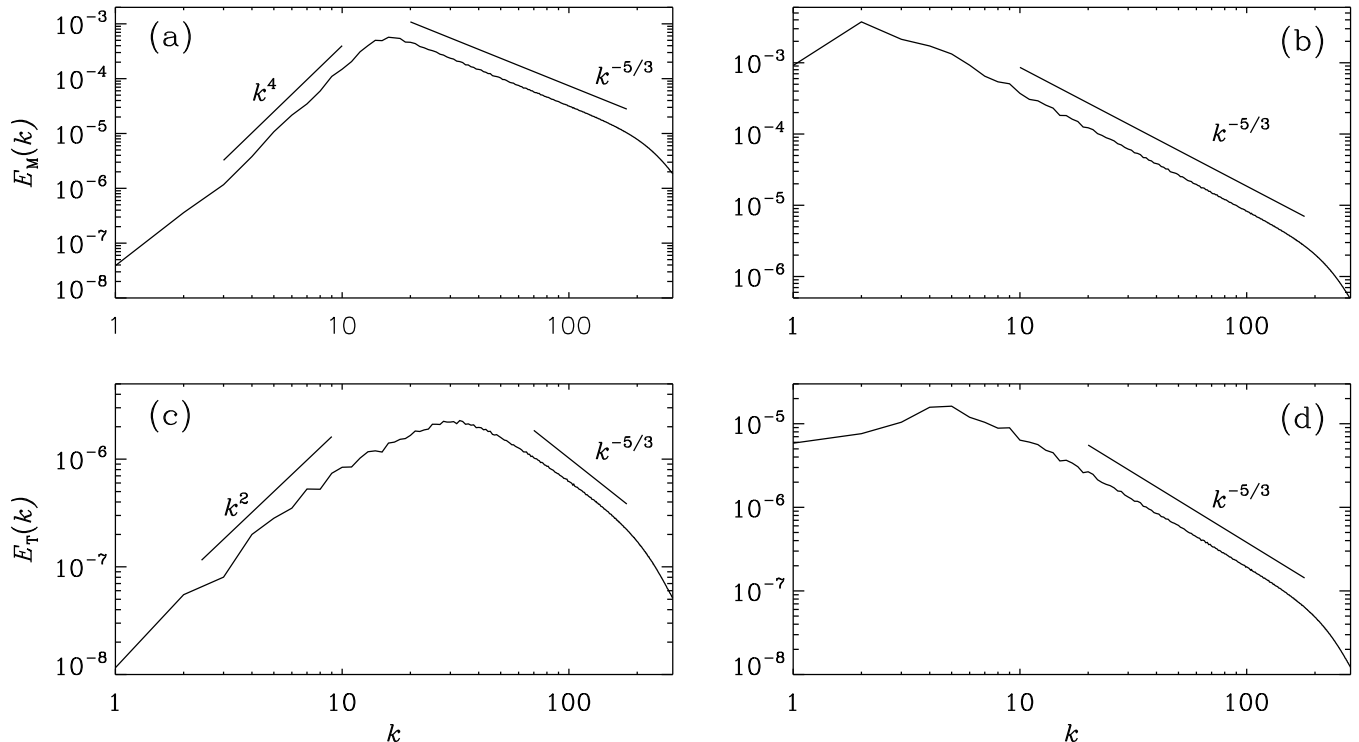


FIG. 6: Spectra of the vector \mathbf{B} , $E_M(k)$, and of the scalar \mathbf{B}^2 , $E_T(k)$, for a random non-helical magnetic field, with spectral peak at $k_* = 15$ (left panels), and $k_* = 2$ (right panels), with amplitude $\Omega_M = 3 \times 10^{-2}$, in normalized units. We see that the magnetic spectrum $E_M(k)$ has the same slope in the inertial range as that of the stress spectrum $E_T(k)$. When \mathbf{B} has a white noise k^2 spectrum or even a Batchelor k^4 spectrum, the spectrum of \mathbf{B}^2 is always that of white noise, i.e., proportional to k^2 .

below unity, so our numerical results have approximately five times smaller strain than the analytical results of Ref. [11]. Their subinertial range slope in $h_c(k)$ is $1/2$ and agrees with ours at very early times; see Section (5). Note that $h_c^2(k) \propto k^{-2}\Omega_{\text{GW}}(k)$. However, after a short time, our spectra gain energy at small k and the spectrum develops a $-1/2$ slope. At high frequencies, our spectrum has a slope of $-7/3$, corresponding to a Kolmogorov spectrum, while that of Ref. [11] has a slope of $-10/3$, which we would obtain if we used a small magnetic Reynolds number, which results in a $k^{-11/3}$ Golitsyn spectrum for the magnetic field Ω_M/k ; see Table II. Note that the spectrum of the magnetic field, and the spectrum of the square of the magnetic field have the same spectral shape in the inertial range. This allows to relate $\Omega_{\text{GW}}(k) \propto k^{-2}\Omega_M$ in the inertial range. However, this is not true in the subinertial range, where the spectrum of the stress is always that of white noise for scalings of the magnetic field steeper than white noise; see Section (3).

TABLE II: Correspondence between the slopes expected from Ref. [11] for the subinertial range (“ana”) and what is obtained in our run ini1 (“sim”), and the results for spectra with the Kolmogorov slope (“Kol”) and the Golitsyn slope (“Gol”), which agrees with Ref. [11].

	slope of ana	sim	Kol	Gol
Ω_M/k	4	4	$-5/3$	$-11/3$
Ω_{GW}/k	2	0	$-11/3$	$-17/3$
h_c	$1/2$	$-1/2$	$-7/3$	$-10/3$

5 Early development of GWs at large scales

We have seen that $\Omega_{\text{GW}}(k, t)/k$ shows a flat spectrum at small k . This might appear unphysical, because it takes some time before power can be established at large scales. In Figure 7 we show that at early times, the spectrum is clearly proportional to k^2 , as expected; see Section (4), and that similar spectra are also being reproduced in 10 and 50 times larger domains. This shows that the flat spectrum is physical and emerges only later.

Figure 8 shows that at small k , $\Omega_{\text{GW}}(k, t)/k$ grows with

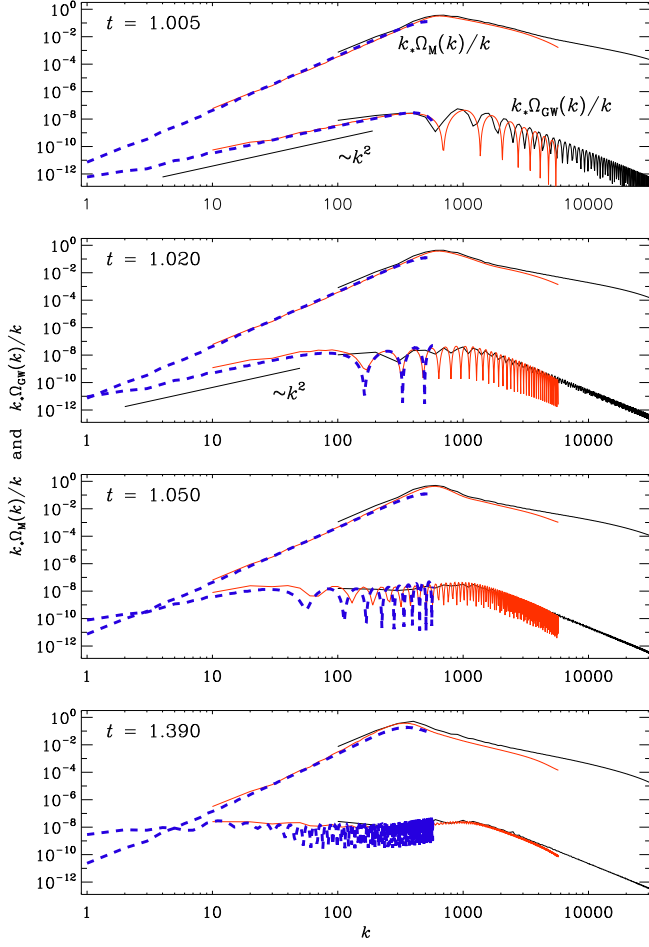


FIG. 7: Magnetic and GW energy spectra amplified by k_* , similar to Figure 1 of the Letter. Also shown in red (blue) are the results for a 10 (red) and 50 (blue) times larger domain. All runs have 1152^3 meshpoints.

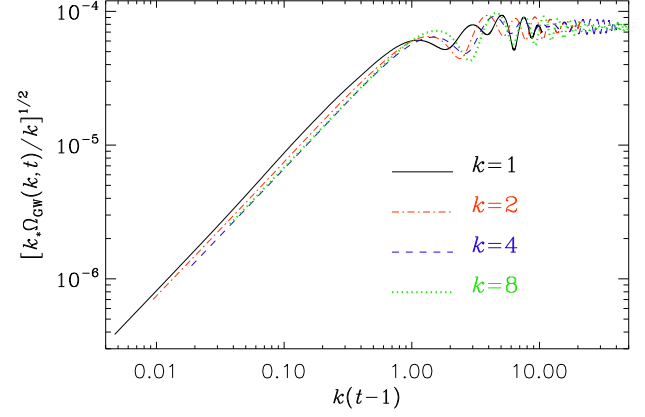


FIG. 8: GW spectral energy versus time for four values of k , demonstrating the k^2 scaling at early times.

t proportional to $k^2(t - t_*)^2$, where $t_* = 1$ in normalized units; see Section (1), and reaches a constant level that is independent of k and is given by the white noise spectrum of the source at large scales. This is demonstrated for wave numbers as small as a few times the Hubble horizon wave number, $k = 1, 2, 4,$ and 8 . A white noise spectrum of the source implies a flat spectrum of $\Omega_{\text{GW}}(k)/k$; see Section (3).